TNO innovation for life

A Quantum Sensing Exploration with Alliander

On Cable Selection and Load Detection

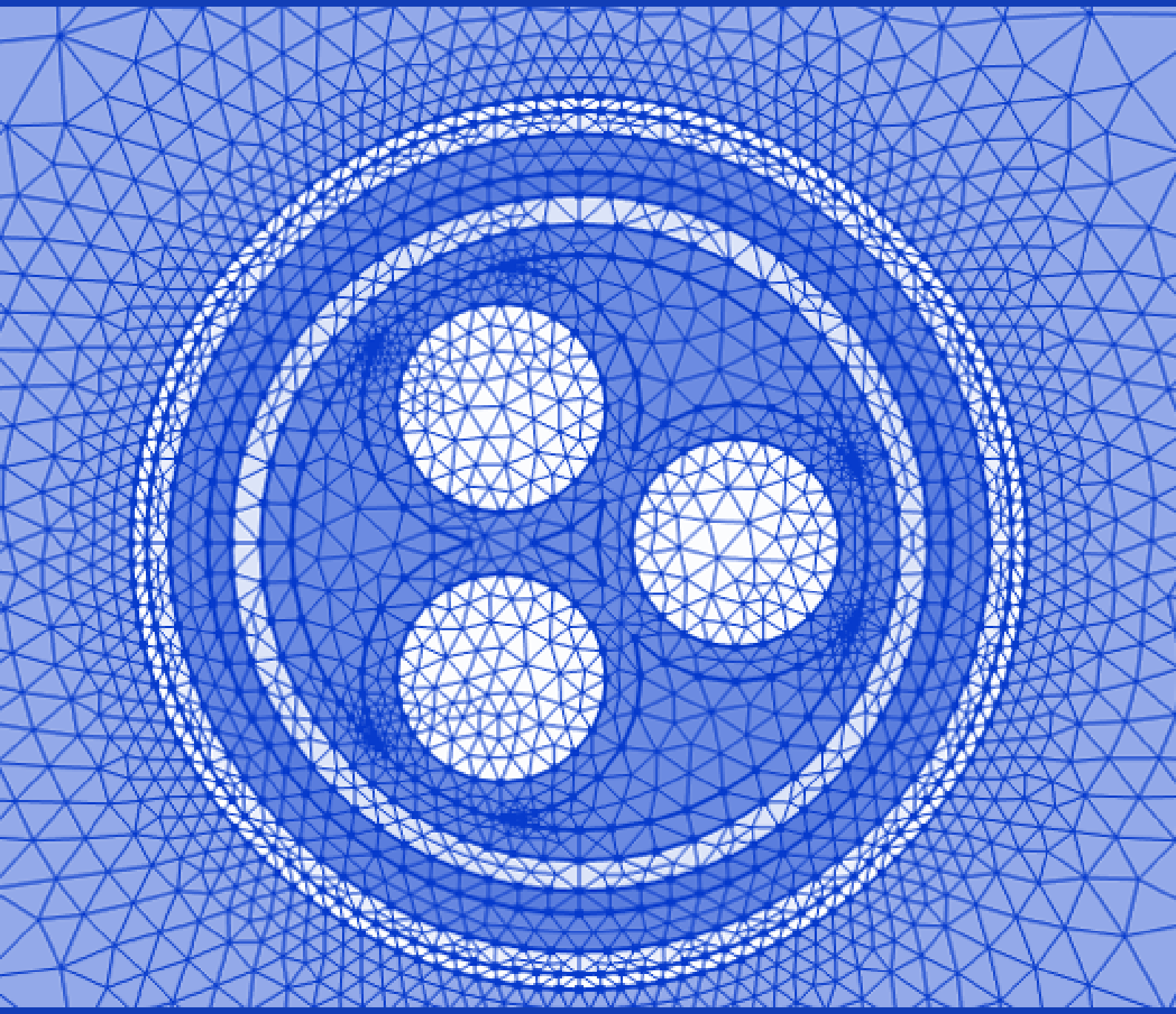

ICT, Strategy and Policy
www.tno.nl
+31 88 866 00 00
info@tno.nl

TNO 2026 R10008 – 27 January 2026

On Cable Selection and Load Detection

A Quantum Sensing Exploration with Alliander

Author(s)	Hans Bartling Simon Cramer Hugo Doeleman Esteban Aguilera
Classification report	TNO Public
Number of pages	39 (excl. front and back cover)
Number of appendices	1

Authors and Contributors

This report was written by

- Hans Bartling, quantum sensing scientist, High Tech Industry Unit at TNO,
- Simon Cramer, quantum application consultant, ICT, Strategy & Policy Unit at TNO,
- Hugo Doeleman, quantum scientist, High Tech Industry Unit at TNO,
- Esteban Aguilera, quantum application consultant, ICT, Strategy & Policy Unit at TNO.

It stems from a collaboration with Alliander, led by the Alliander Research Center for Digital Technologies. Contributors from Alliander include

- Nikki Jaspers,
- Milou van Nederveen,
- Jelte Zwetsloot,
- Bert van Norden,
- Dirk Köning,
- the Energy Fraud team.

The lab and field measurements were done using the quantum magnetometer developed at TNO within the Quantum Sensing Testbed, supported by Quantum Delta NL.

Contents

1 Introduction

The energy transition in the Netherlands is in full swing. Energy network companies such as Alliander are trying the best they can to keep up with all the challenges that the energy transition brings. The most obvious challenge is that the capacity of the energy grid needs to be increased, almost doubled in only ten years of time. This is an enormous task, and grid operators are already behind schedule. Bottlenecks are arising everywhere, slowing down both the energy transition and other societal projects such as the building of housing. The number of bottlenecks will keep increasing if we don't look at new solutions.

There are many approaches to choose from and experiments to perform to find these new solutions. One of the essential tracks is concerned with increasing the efficiency of current processes related to maintaining the electricity cables within the grid. These cables are often below the surface, which introduces various challenges, two of which we consider in more detail: **cable selection** and **load detection**. Both are considered with measuring the magnetic field of a cable to infer properties of the cable. For cable selection, the measurements take place in close proximity to the cable, i.e., in a trench that has been dug open and where now a technician needs to identify the correct cable for their job. For load detection, the measurements take place above ground, so with a larger distance to the cable, and the technician wants to identify how much current is running on the underground cable.

The aim of this project is to investigate the current methodologies and processes related to cable selection and load detection, as well as exploring the applicability of quantum magnetometers to these challenges. Quantum sensing is of interest because certain quantum magnetometer modalities can offer combinations of high sensitivity, vector capability, and bandwidth that may be valuable in specific use cases, e.g., weak signals, or challenging electromagnetic environments with various noise factors. The important questions to answer here are:

- Where do classical sensors suffice and the limitations are actually somewhere else?
- And where could quantum sensors add distinct operational value?

This report is structured as follows. We first focus on cable selection in Chapter 2 and use finite element simulations to study magnetic fields close to a cable, leading to practical insights and recommendations as well as a comment on the applicability of quantum sensors. Chapter 3 focuses on load detection, where we model expected magnetic fields further away from the cable and showcase methods to infer current and depth from above ground measurements. We again conclude with summarising our insights and comment on the applicability of quantum magnetometers. Chapter 4 describes the lab and field tests we have conducted with the NV-based quantum magnetometer we develop at TNO in Delft. Finally, we give a summary of the work and combine the different insights gained from desk research and experiments.

2 Cable Selection

2.1 Problem definition

The methods currently being used for cable selection require a technician to head to the closest secondary substation (where cables are identified) to connect a signal transmitter device to the correct cable. This transmitter sends 1 ms pulses of DC current of 300 V, 300 A, every 4 seconds.

This signal can be found using a receiver at the job site, which has either a loop or a spool as a sensor head, depending on which method is used. The following are known issues that can occur with these methods:

- The loop ('LUS') method (transmitter connected to phase/ground)
  - There is a cable in the ground that has some small return current, which can appear to be the right cable because the technician increased the gain.
  - The signal is sensitive to where the loop connector is placed (rotating the loop changes the measurement outcome).
  - If there is no significant change in the current, the method can be inconclusive.
  - It is sensitive to interference, e.g., from train lines, because it always needs a connection to ground.
  - The calibration is not done on the full cable but on a breakout, which is not always representable for the entire cable.
- The spool ('SPOEL') method (transmitter connected to phase/phase)
  - The spool method could work fine in all situations, but is not always used because of the wide adoption of previous practices.
  - The incidents that remain are due to incorrect operation rather than hardware limitations. The technician may turn up gain too high, for example.
  - Measuring a cable is somewhat time-consuming, as one has to wait for the pulses and rotate the sensor multiple times (for each phase).

For both methods, a common issue is the required time-consuming trip to the secondary substations.

While selecting the wrong cable in general is clearly undesired, most risks arise when there is confusion between low- and medium-voltage cables, which can mainly happen for paper-insulated lead-covered (PILC) cables, as they typically look identical.

2.2 Understanding magnetic fields close to the cable

Any approach to cable selection (or load detection) will leverage either the electric or magnetic fields generated by the cable signals. It is therefore imperative to understand the shape and magnitude of these fields. Although the fields from a single unshielded wire can be easily obtained from, e.g., the Biot-Savart law, the presence of three phase wires and the metal shields around them complicate such analytical predictions. In particular, the electric fields

are strongly shielded and reshaped by the conductive shields (any metal), while the magnetic fields are mostly affected by shield materials with high magnetic permeability, like steel. We therefore decided to perform a finite element simulation of the electric and magnetic fields close to a power cable. The simulation is done in COMSOL Multiphysics, a commercial simulation software package.

These simulations reveal both the magnitude and the symmetries of the electromagnetic fields. The magnitude of the fields around the cable is crucial to the feasibility of electric or magnetic selection and detection schemes. From the same simulation, we can assess whether the fields retain certain symmetries of the wire arrangement inside the cable.

We chose to simulate an example of a **paper-insulated lead-covered (PILC) medium-voltage cable**. These are especially interesting, because, for PILC cables, medium- and low-voltage cables cannot be distinguished by eye. Moreover, because of their steel jacket, these cables will create magnetic fields lower than those of modern XLPE cables. Thus, this serves as a worst-case scenario.

We will first discuss the geometry and physics used in the simulation, before moving on to the simulation results and their interpretation. After that, we propose a metric to measure the symmetry of a cable to learn about its arrangement.

2.2.1 Setup of COMSOL simulation

Our simulation is an adaptation of a simulation from a COMSOL cable tutorial [1].

Geometry, materials and mesh for the simulation

As discussed above, we model a MV PILC cable. We use the translational symmetry of the cable to perform the simulation in the 2D plane of the cable cross-cut. Figure 2.1a shows the geometry of the simulation. The geometry is inspired by that of a 150 mm^2 PILC cable with layer structure as shown in Figure 4.1 of Phase-to-Phase [2]. The three phase wires each have a cross-section of 150 mm^2 and are made of aluminium. They are each isolated by a mass-impregnated paper (MIP) jacket, and the bundle is isolated by several layers of cable isolation and shielding. Insulator layer thicknesses vary between 1 and 2.5 mm. Lead and steel thicknesses are 2 and 1.5 mm, respectively. The total diameter of the cable is approximately 59 mm, matching the specifications provided by a supplier [3]. The cable is surrounded by a 59-mm-thick shell of air in the simulation, which we estimate to be a sufficiently large domain to study our fields of interest without unnecessarily increasing computation time. As discussed in the next section, the boundary conditions at the edge of the simulation domain are chosen to approximate a continuation to infinite free space.

The materials are defined by their relative magnetic permeabilities μ_r and relative dielectric permittivities ϵ_r or (for conductors) conductivities σ. In table 2.1 we show the values used for the materials in this simulation. Particularly important to the resulting magnetic fields is the permeability of steel, which is the only material that contributes significantly to magnetic shielding. This value was taken from the standard value for galvanized steel in the COMSOL material library, but in the literature a range of values between $\sim$100 and $\sim$8000 can be found. We therefore expect that the type of steel will have a large influence on the magnitude of the fields outside the cable.

Figure 2.1b shows the geometry after meshing. We used a physics-controlled mesh with element size set to ‘Normal’.

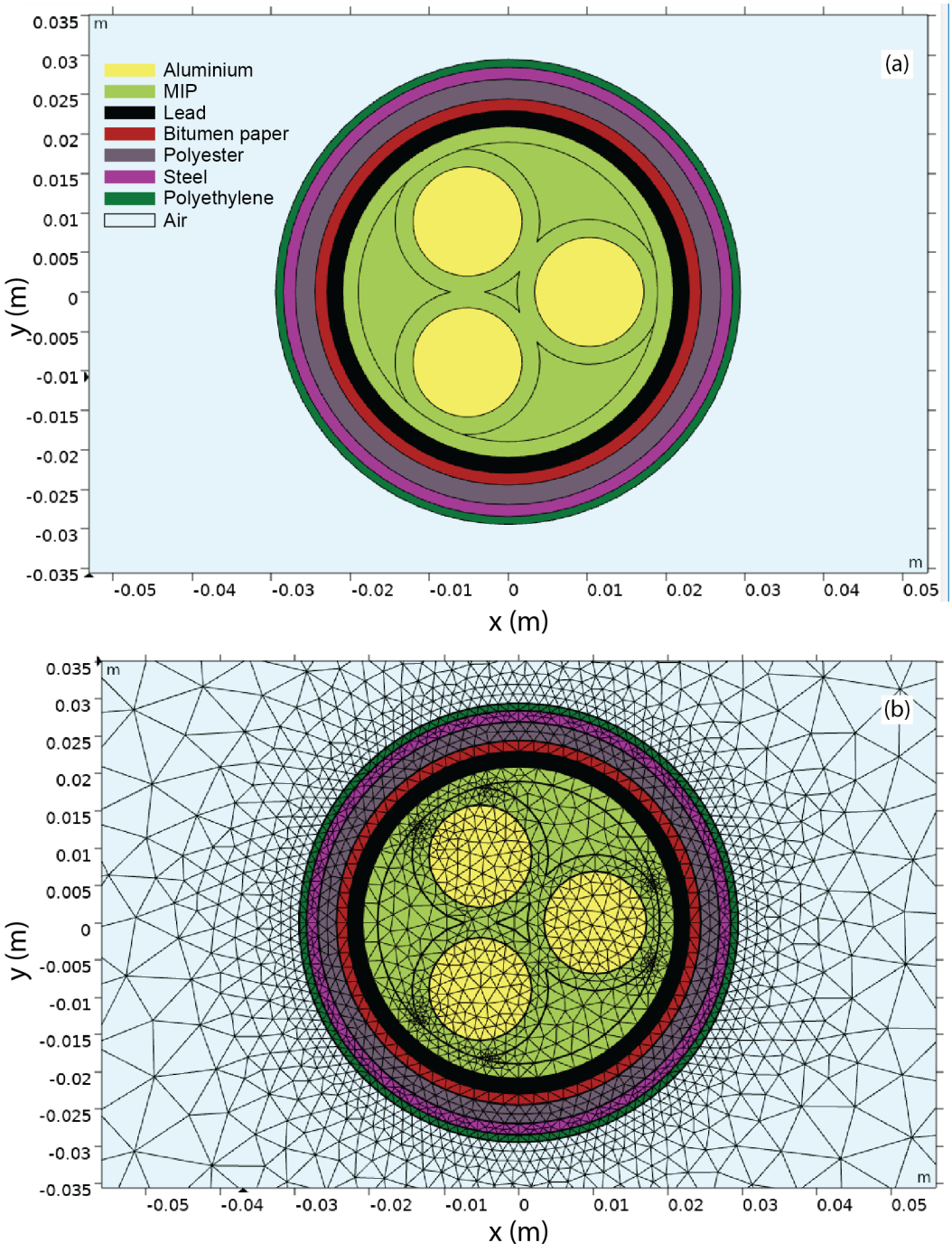

Figure 2.1: **Geometry and mesh of the finite element simulations. (a)** Cable geometry, zoomed in on the cable. We see the 3 aluminium cable cores (yellow) and the phase isolation of mass impregnated paper (MIP, light green). The cable isolation layers, from inside to outside, are MIP (light green), lead (black), bitumen paper (dark red), polyester cloth (grey), steel (purple), and polyethylene (dark green). Outside the cable is taken to be air (light blue). The voids filling the spaces between the phase wires and the cable isolation layers (light green) is taken to be MIP as well. **(b)** Meshed simulation domains.

Material	ϵ_r	μ_r	σ (S/m)
Aluminium	1	1	$3.774 \cdot 10^7$
Mass impregnated paper (MIP)	3.6	1	10^{-18}
Lead	1	1	$4.55 \cdot 10^6$
Bitumen paper	3.16	1	$3.2 \cdot 10^{-9}$
Polyester cloth	1.9	1	10^{-18}
Steel	1	100-50j	$1.46 \cdot 10^6$
Polyethylene	2.25	1	10^{-18}
Air	1	1	10^{-14}

Table 2.1: Material parameters used in the simulation of a PILC cable.

Physics interfaces and study

Our simulation uses two physics interfaces: the magnetic fields (mf) and the electric currents (ec) interface. The first is suited to compute magnetic fields in and around conductors with specified currents, and the second produces electric fields, induced currents and potentials in conducting media for specified voltages on nearby conductors.

To condition the magnetic fields interface, we set the three phase wires to carry sinusoidal currents at a frequency of 50 Hz, a peak current of 100 A and with 120° phase difference between each wire. This frequency and phase difference is standard for all MV 3-phase cables used by Alliander, while the current strength can range between 0A to 250A per phase, so we chose a value in the middle. The outer boundary of the simulation domain is set to be magnetically insulated, which simulates infinity for magnetic fields (i.e. avoiding reflections at the boundary). To condition the electric currents interface, we set the three phase wires to carry voltages in phase with the currents and with a peak (phase-to-ground) voltage of $10/\sqrt{3}$ kV, according to typical values seen in MV cables. The simulation domain boundary is set to ground, and the various conductive cable shields are left floating.

We then perform a frequency domain study, which means we fix the frequency of the oscillating currents and voltages to 50 Hz and simulate the resulting harmonic fields. The solution is obtained for any desired electrical phase θ, i.e., any point in the harmonic cycle.

2.2.2 Results

Here we present the field distributions obtained from the COMSOL simulations.

Field snapshots

Figure 2.2a and b show the electric potential and field, respectively, at a snapshot in time corresponding to electrical phase $\theta = 0°$. At this point, the top left cable is at maximum voltage. A snapshot of potential at $\theta = 120°$ shows the same picture, but rotated clockwise by 120° to have the rightmost cable at maximum voltage. This fact is at the heart of the three-fold symmetry of the fields in these cables: a progression in phase by 120° produces a field plot that is rotated in space compared to the initial situation by 120°, and similar with 240°. We will discuss that in more detail in section 2.3. Moreover, from the magnitude of the field in Figure 2.2b we can see that the two conductive shields (lead and steel) very effectively contain the electric field to inside the cable. The electric field outside the cable is roughly 1 mV/m, while it is more than 300 kV/m just inside the lead shield.

It is worth noting that cable shields may sometimes be grounded at mid stations. In that case, if the ground connection is good and one measures near a mid station, no electric field at all

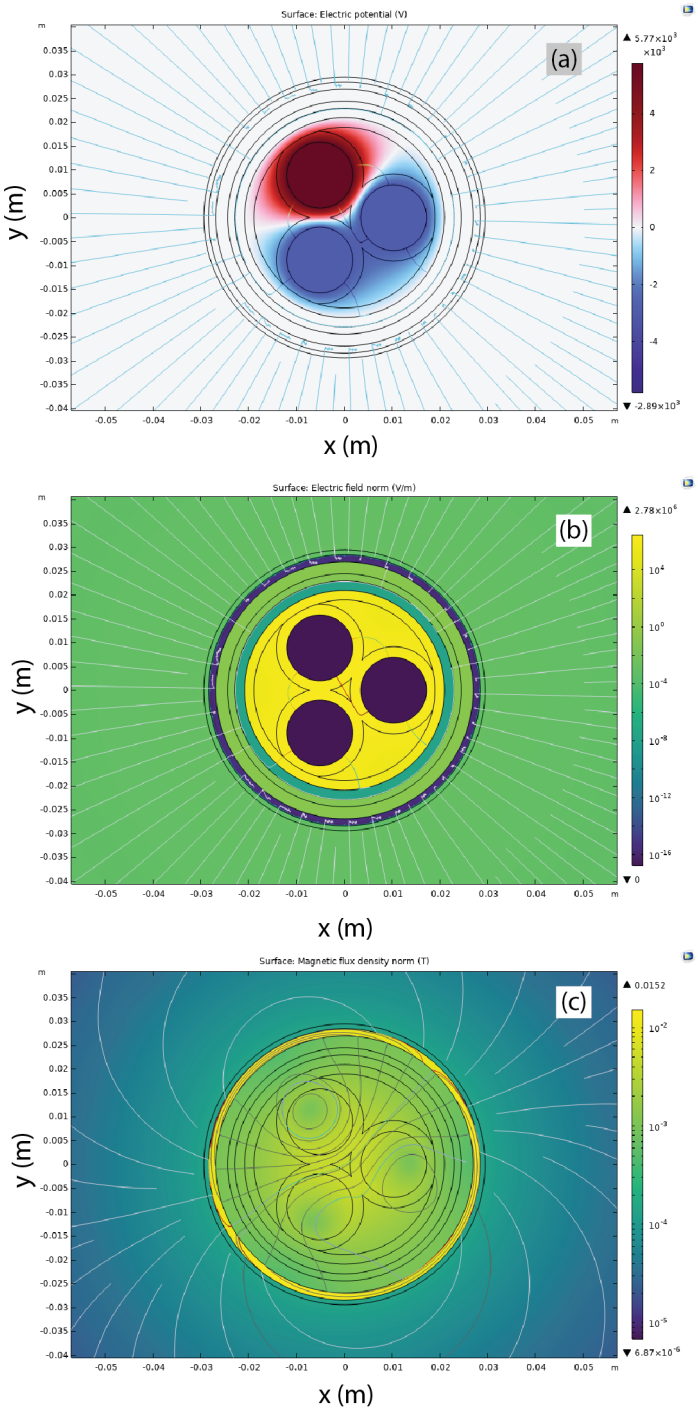

Figure 2.2: **Snapshots of potential and fields at $\theta = 0°$. (a)** Electric potential, linear scale. At $\theta = 0°$, the voltage (and current) on the top left phase wire is maximal, while the other two wires are at phase $+120°$ and $-120°$. The colour map shows potential, while the lines follow electric field direction. **(b)** Electric field norm, logarithmic scale. As in (a), lines are electric field lines. We see that the conductive shields reduce the electric field outside the cable in two stages by 8 orders of magnitude, and make electric field uniform around the cable. **(c)** Magnetic field norm, logarithmic scale. The magnetic field in the cable penetrates unchanged through all layers except the steel, which has significant permeability and attenuates the field outside the cable by roughly a factor 5.

is expected outside the cable.

Figure 2.2c shows the magnetic field norm (i.e., the magnetic flux density), also at $\theta = 0°$. In contrast to the electric field, the magnetic field is only weakly shielded by the cable layers. Only the steel layer reduces the field outside it compared to inside, but just by a factor 5. The field at the cable surface is still roughly 100 µT. From discussions with Milo Kluver at Alliander, we learned that for the field calculations they do, they use an empirical 'damping' factor of 50% to match the fields calculated analytically from unshielded phases to experimentally measured values. Our factor 5, so a reduction to 20%, is therefore likely an overestimation. We also note that if shields are made of very good conductors, magnetic fields may also be suppressed by eddy currents. We tested this by increasing the lead conductivity to very high (unrealistic) values, which caused the magnetic fields to disappear outside the cables.

Time-averaged fields

The snapshot of the potential in Figure 2.2(a) shows a clear three fold symmetry, however, the snapshots of the magnetic fields outside of the cable do not clearly show that, as visible in Figure 2.2and (c). Here, we will look at time-averaged fields to see if these reveal that symmetry.

Averaging fields at different snapshots in time cannot be done directly in COMSOL, so we instead perform this post-processing in python. From COMSOL, we export a dataset with 360 snapshots corresponding to $\theta = 0°, 1°, 2°, ...$ We export B_x and B_y, i.e., the x- and y-components of the magnetic field. In python, we compute from these B_r, B_ϕ and B_{tot}, the radial component, azimuthal component and norm of the field, respectively, at each snapshot. Then we calculate the root mean square (RMS) value of the fields, taken over all snapshots, to get an RMS field at each point in space.

Figure 2.3 shows the RMS field maps. As shown in fig. 2.3a, the fields inside the cable are so much larger than outside it that the variation outside is not visible on the same colour scale. We therefore mask the inner fields in panels b-d to better see the field variations outside. From fig. 2.3b we see that the total field is on the order of 100 µT, as also seen from the snapshot earlier, which is easily measurable with most magnetic field sensors. The field now also shows three-fold symmetry, as expected and in contrast to the snapshots in fig. 2.2. Moreover, if one considers the field at a fixed radius slightly outside the cable, the contrast between maximum and minimum fields at different azimuthal positions is roughly a factor 2. This means that it should be easily measurable by a small magnetometer, measuring at different positions around the cable, whether the cable fields show three-fold symmetry.

Magnetic field sensors do not (directly) measure total field but rather one or multiple field components. Figure 2.3a and b therefore show B_r and B_ϕ, respectively. We see that B_ϕ dominates and peaks at the phase wire positions, while B_r is somewhat smaller and peaks in between the wires. The minimum-maximum contrast at constant radius slightly improves if we consider only one field component.

2.3 Symmetry metric

Unlike low-voltage cables, medium voltage cables contain 3 phase wires arranged in a triangle and carry well-balanced currents at 120-degree phase difference. As we have seen above, this creates measurable three-fold symmetric (time-averaged) field profiles. In contrast, low-voltage cables contain a fourth 'zero' wire, which may also carry some current, and the three-phase currents are typically not well balanced (i.e., they do not add up to zero). Hence, no

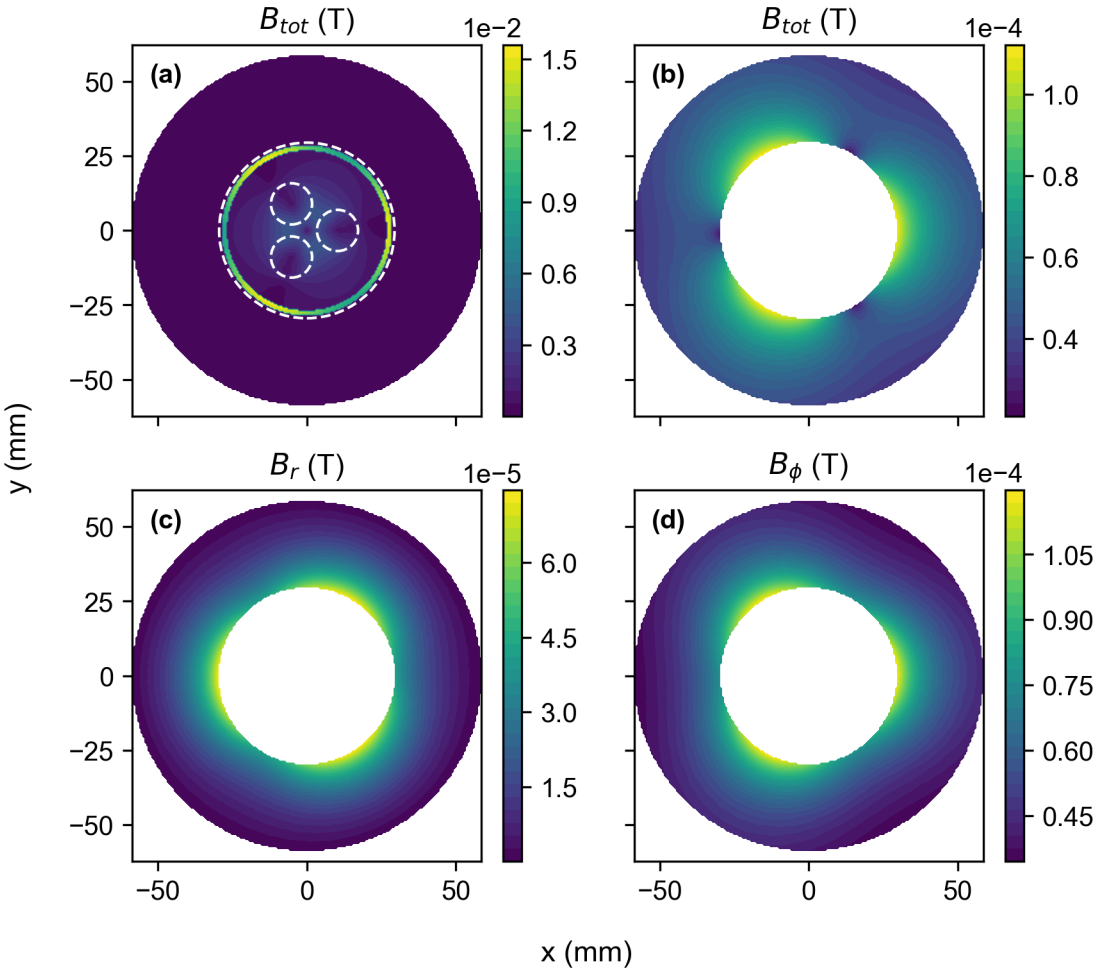

Figure 2.3: **RMS values of magnetic fields. (a)** Total magnetic field in and around cable. Dashed lines show the outer contours of the cable and the three phase wires. **(b)** Total magnetic field around the cable only. **(c)** Radial component of magnetic field around the cable. This peaks at the locations between the phase wires. **(d)** Azimuthal component of the magnetic field around the cable. It peaks near the phase wires and is stronger than the radial component, dominating total field. Three-fold symmetry is visible in all the field components.

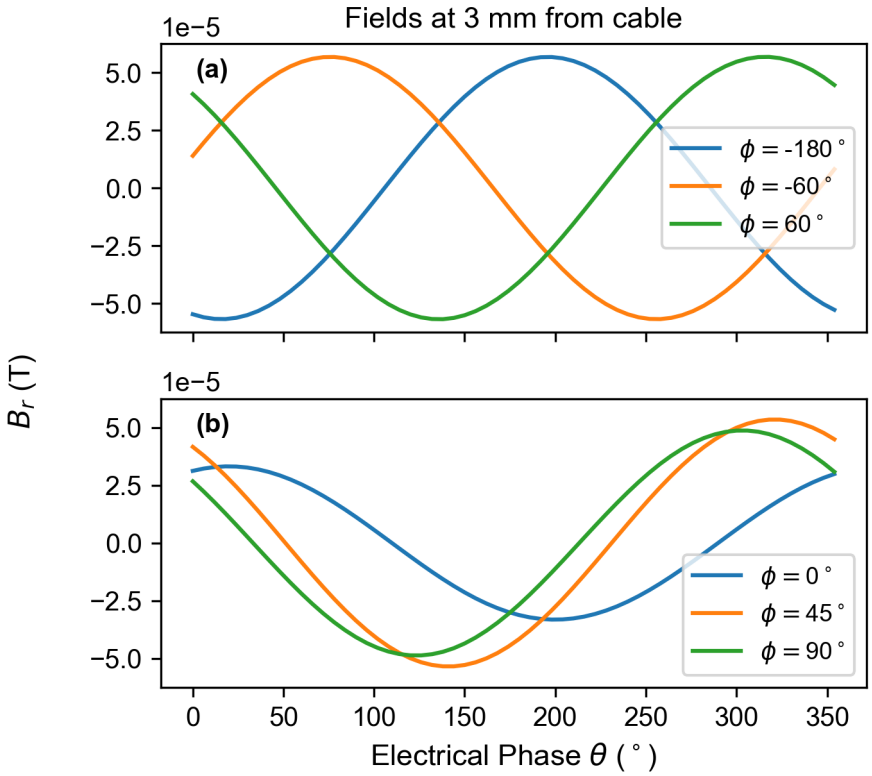

Figure 2.4: **Sensor signals for three sensors placed at different azimuthal positions.** We show radial magnetic field components B_r as a function of electrical phase θ (i.e. time), as they would be measured by radially oriented magnetic field sensors placed at 3 mm from the cable surface and different azimuthal positions ϕ. **(a)** Sensors spaced by 120° show equal signals, with a phase delay of 120°. **(b)** Sensors spaced by different angles (45° in this case) do not show such symmetry. This can be interpreted as a proxy for sensors spaced by 120° on a cable without three-fold symmetry.

three-fold symmetry is expected. In this Section, we define a symmetry metric that could potentially help to distinguish MV and LV cables.

Time-dependent sensor fields

While three-fold symmetry is already apparent from the RMS fields discussed in the previous section, there are methods to distinguish three-fold symmetry which produce better contrast, and so easier distinction between LV (non-symmetric) and MV (symmetric) cables. This involves making use of our knowledge of the relative phase differences of 120° between the currents in the three phase wires. As mentioned in Section 2.2.2, a progression in phase by 120° produces a field plot that is rotated in space compared to the initial situation by 120°, and similarly with 240°. Here we visualize this through the fields that a sensor would measure at different positions along the cable circumference. We then propose a metric to distinguish symmetric and non-symmetric cables.

A sensor device that aims to distinguish MV and LV cables by the symmetry of their fields could consist of three magnetic field sensors arranged on a ring surrounding the cable. These sensors should be separated by azimuthal angles of $\delta\phi = 120°$. Figure 2.4 shows fields as they would be measured by these sensors. We assume the sensors measure radial field components, but the same conclusions could be drawn for azimuthal field components. All sensors are placed

at the same radial position, corresponding to 3 mm outside the cable. In Figure 2.4a, we show the fields for sensors separated by $\delta\phi = 120^\circ$, which are equal up to a phase shift $|\delta\theta| = 120^\circ$. This is the result of the three-fold symmetry in the phase wire arrangement. We note that this relation will hold for any set of 3 positions ϕ_1, ϕ_2, ϕ_3, provided that the spacing is 120°.

The same phase-shifted signal symmetry will not be present in cables without three-fold symmetry, like LV cables. To show this directly would require a simulation of such a cable. However, we can mimic this situation by simply placing our sensors at any other angular separation than 120°. Sampling a three-fold symmetric field at these non-symmetric points is similar to sampling a non-symmetric field at points separated by 120°. Figure 2.4b shows the fields for this situation, here placing the sensors at $\delta\phi = 45^\circ$ angular separation. No symmetry between the fields is apparent.

Defining a symmetry metric

From the measured sensor fields, our sensor device could calculate a single metric that distinguishes symmetric and non-symmetric fields. This metric should ideally be 1 for symmetric fields, and 0 for non-symmetric fields (or vice versa). We propose the following metric M, which we could define as a 3-fold phase-delayed cross-correlation.

For each sensor signal $s_j(t)$, with $j \in 1, 2, 3$, we compute the complex Fourier coefficient at frequency $f_0 = 50$ Hz as

$$S_j = 1/T \int_0^T s_j(t) e^{-2\pi i f_0 t} dt = A_j e^{i\Phi_j}, \tag{2.1}$$

with T the measurement time (at least $1/f_0 = 20$ ms). The phase Φ_j will contain the relative phase delays between the signals. Now we define two numerators as

$$C_+ = \frac{1}{3}\left(S_1 + S_2 e^{2\pi i/3} + S_3 e^{4\pi i/3}\right) \tag{2.2}$$

$$C_- = \frac{1}{3}\left(S_1 + S_2 e^{-2\pi i/3} + S_3 e^{-4\pi i/3}\right). \tag{2.3}$$

In the perfectly 3-fold symmetric case, the 3 signals will be equal but phase delayed by either 120° or -120° (depending on how the sensors are placed with respect to the phase wire ordering), such that, in the first case,

$$S_1 = Ae^{i\Phi}, \quad S_2 = Ae^{i(\Phi - \frac{2\pi}{3})}, \quad S_3 = Ae^{i(\Phi - \frac{4\pi}{3})}, \tag{2.4}$$

which leads to

$$C_+ = Ae^{i\Phi}. \tag{2.5}$$

Now we define the symmetry metric M by normalizing the maximum of the two numerators by the maximum possible numerator as

$$M = \frac{\max\left(|C_+|, |C_-|\right)}{\sqrt{\frac{1}{3}\left(|S_1|^2 + |S_2|^2 + |S_3|^2\right)}}. \tag{2.6}$$

This metric equals 1 for either 120° or -120° phase symmetry, < 1 otherwise and 0 in the limit of completely uncorrelated signals. It is insensitive to the global signal amplitude or phase and can be computed rapidly, for example using a fast Fourier transform (FFT).

To demonstrate how the symmetry metric performs for signals with and without phase-delayed symmetry, we sample the radial field B_r at 3 positions with fixed radial

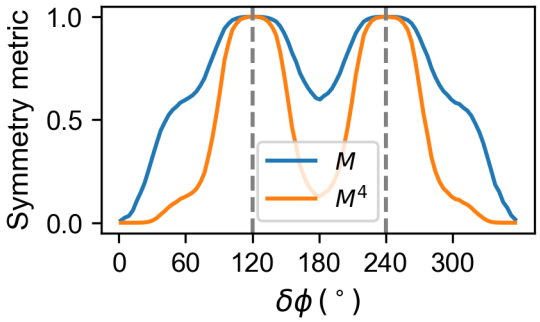

Figure 2.5: **Symmetry metrics for different angular sensor displacements.** Dashed lines at 120° and 240° show where the signals are expected to have perfect phase-delayed symmetry.

coordinate and 3 different azimuthal coordinates regularly spaced by $\delta\phi$. Examples of such signals were shown in Figure 2.4 for $\delta\phi = 120°$ and $\delta\phi = 45°$. Figure 2.5 shows the symmetry metric M as function of $\delta\phi$. Only at $\delta\phi = 120°, 240°$ do the signals have phase-delayed symmetry, and indeed we see that M reaches 1 there. For other azimuthal spacings such symmetry is absent and the metric drops. While M does not drop very steeply as we move away from the symmetry points, one can use instead a higher power of M as a more 'critical' judge of symmetry, as can be seen from the curve for M^4.

2.3.1 Measuring the symmetry to distinguish LV and MV cables

In this Section we want to discuss how one could incorporate the symmetry of the cable to distinguish between LV and MV cables.

As a baseline, one could use the time-averaged fields we discussed in Section 2.2.2. This suggests a first, conceptually simple approach to assess symmetry for an unknown cable: take a single sensor and scan it along the cable circumference, recording RMS field values. The advantage of this approach is that it requires only a single sensor. In practice, it may be difficult to record azimuthal position though.

This is where the symmetry metric M (or higher powers of it) could provide benefits. One could envision an approach based on 3 sensors placed 120° apart on a ring centred on the cable. Their signals can be used to compute a symmetry metric that can inform on the presence of (the right kind of) symmetry in the cable to distinguish MV and LV cables. We suggest one metric M, but others are possible (such as higher powers of M). To assess what is the most suitable metric, an experimental test with MV and LV cable fields would be necessary. Such tests should also assess how robust this metric is to ,e.g., small sensor displacements from perfect 120° spacing, imperfect centring of the sensor ring and clumps of dirt on the cable. The advantage of this method is that, because it also uses the known delay between the signals from the 3 phase wires, it can be more sensitive to the expected symmetry. Making a ring with 3 sensors may also be easier than making a device to track azimuthal position of a single scanning sensor.

In a real cable selection situation, there will be other cables nearby, producing background fields. These may distort the symmetry we seek to assess. This should be taken into account when defining a robust metric. It may also be that adding additional sensors will allow to separate such background fields (which have low gradients) from the cable-of-interest fields

(which have higher gradients as this cable is closer). For example, instead of using 3 sensors we could use 3 pairs of sensors, where sensors in each pair are placed close to each other. Background fields are expected to be the same in each sensor within a pair, so can be removed by taking the difference between the signals from two sensors in a pair. Cable fields, however, have larger gradient, so will lead to a finite value in this difference signal.

2.4 Insights and recommendations

In this section, we discuss our findings and give suggestions on how to potentially improve current processes. These suggestions come from our technical point of view and might not always be fully applicable to the operational scenarios encountered at Alliander. We will discuss some 'straight-forward' improvements (at least straight-forward from a technical perspective), as well as more involved insights for distinguishing LV and MV cables, capacitive currents, and possibilities with smart secondary substations. Most suggestions do not immediately necessitate the use of quantum sensors, so we discuss the applicability of quantum sensors for cable selection separately at the end of this section.

2.4.1 'Straight-forward' improvements

- **Digital readout on sensor.** The current handheld magnetometers that are used to detect the signal on the cable have an analogue display that can max out. This can lead to wrong readings of the signal strength, especially when the signal is stronger than the maximum signal that can be displayed. There could be a benefit in having a digital display that shows actual values to reduce ambiguity.
- **Switching to AC signals.** The typical cable selection procedure works with short DC pulses every 4 seconds. That means that the technician has to wait for pulses every time they measure, which can add up if they have to measure multiple cables with multiple phases. For currently used cable colouring and cable detection methods, the signal that is put on is a distinct AC frequency, typically in the kHz range, which can be detected by the sensor. Such an approach could also be beneficial for cable selection methods, as the 'waiting for pulses' is eliminated and kHz frequencies will also not be significantly interfered with by other surrounding sources, which are typically running at 50 Hz.
- **'Navigating' towards the right cable.** By straightening the loop and using it as a sort of antenna, a skilled technician is currently able to 'navigate' towards the correct cable. This requires a good understanding of the magnetic fields and general experience with cable selection processes. To make this process easier for the technician, especially for less experienced colleagues, one could imagine a sensor head that includes not one but 3 magnetometers, which can be used to determine the vector component of the magnetic field and translate this to a clear sign (e.g., an arrow pointing towards the correct cable) on the display.

2.4.2 Distinguishing between LV and MV cables

- **3- vs. no or 4-fold symmetries.** As discussed in Section 2.3, low-voltage and medium-voltage cables differ by the amount of wires in them, which could make them distinguishable through magnetic field measurements. We described methods on how to do this and proposed a metric to use. In practice, such a method would help to ensure that a medium voltage cable is not mistaken for a low voltage cable and then cut while under load,

leading to potentially serious accidents. With the proposed methods, we cannot envision situations where this could happen, given the assumption that medium voltage cables truly always have well-balanced current on all 3 phases (which is true as far as we understood the technicians from Alliander) and there are no measurement errors. We could imagine, however, that a low voltage cable is mistaken for a medium voltage cable when there are loads on the 4 wires which coincidentally closely resemble the 3-fold symmetry expected from a medium voltage cable. Such a mistake would generally not be dangerous, as we mistake the 'safe' cable for a 'dangerous' cable, and hence the technician would not do any cutting on it. However, not finding the correct cable could lead to frustrations, which could in turn lead to poor decision making, which could create unsafe situations.

- **Electric fields.** Another distinguishing property is the difference in electric field strength induced by the difference in voltages. However, as discussed in Section 2.2.2, we saw that electric fields outside cables are on the order of 1 mV/m, which is very challenging to measure. In fact, we do not know of any sensor that can measure such small electric fields. We note that this field strength depends strongly on the conductive shield thicknesses and conductivities. Given that the shields used in this simulation were steel and lead, which are far less conductive than the copper shields used in modern XLPE cables, we do not expect electric fields to be measurable for any relevant shielded cables.

2.4.3 Capacitive currents on connected cables

As a safety measure, Alliander would like to be able to determine in the trench if a cable is connected or disconnected at the secondary substation. Cables act like long capacitors, where the changing voltage from an AC power source causes small capacitive currents to flow in the cable. If the connected cable has no load on it but there is still a voltage applied, one could potentially distinguish such a cable from a fully disconnected cable through measuring the magnetic fields induced by capacitive currents. This is not currently done by Alliander, so we would like to give some purely theoretical considerations in this section.

Capacitive current is given by

$$I_C = U \cdot 2\pi f \cdot C, \tag{2.7}$$

where U is the operating voltage in Volt, f is the AC frequency in Hz, and C is the capacitance of the cable in F/km. We consider low and medium voltage XLPE cables here, with 400 V and 10 kV applied respectively. The capacitance for these cables is typically somewhere between 0.1 µF/km and 0.8 µF/km, see e.g. [4].

I_C	0.1 µF/km	0.8 µF/km
LV: 400 V	12.6 mA/km	100.5 mA/km
MV: 10 kV	314.2 mA/km	2513.3 mA/km

Table 2.2: Capacitive currents for low and medium voltage XLPE cables.

Note that the capacitive current is given in mA/km, so the actual currents depend on the length of the cable. We assume a length of 1 km. We can estimate the magnetic field around a cable based on these currents using the python simulation we made. Considering the smallest current, i.e., 12.6 mA, the resulting magnetic field for a 3-phase balanced cable would be around 0.5 nT at 10 cm distance to the cable centre. Realistic measurement outcomes would further depend on how well the phases are actually balanced (resulting in stronger fields for less well-balanced cables), how long the cable is (a shorter cable results in smaller magnetic fields), and how well the shielding of the cable works (however, Alliander technicians assume only a 50% dampening).

Given these considerations, we can assume that the relevant magnetic fields can in some cases be quite small, around single digit nT, which could require sophisticated sensors to detect.

2.4.4 Possibilities with smart secondary substations

We would like to briefly comment on the possibilities if the relevant secondary substations are 'smart' secondary substations, which refers to stations where the power lines are monitored and parameters like load and/or frequency are communicated via the Internet. It is not entirely clear what monitoring functionalities would be available, so we are making some assumptions here.

One could envision a sensing device at the trench that has access to the data output from the secondary substation. The sensor could then measure the magnetic field of a cable, infer the current as well as, e.g., the precise frequency of the signal, and compare these measurements with the data output of the secondary substation. This should not be a snapshot measurement, but rather a measurement over a short time span to ensure high confidence when deciding which cable is being measured. The device could continuously compare with the data of all relevant cables at the secondary substation until the confidence is high enough and then give an output to the user. Depending on the variability of the signals on the different cables, this process could be very time efficient. To speed things up, one could also envision a device with multiple sensor heads that can be connected to multiple cables at the same time.

The improvements with this method are not only a potentially faster and more accurate identification of the cable in the trench compared to the pulsed-signal method, but rather also in saving the trips to the secondary substation to connect the pulse source.

2.4.5 Applicability of quantum sensors

As we have seen in Section 2.2.2, the fields in close proximity to the cable are of sufficient magnitude ($\sim$100 µT) that most magnetic field sensors can accurately measure them. In fact, it is similar to the earth magnetic field, so any compass sensor could be used if it can resolve 50 Hz. This does not require a quantum sensor of exquisite sensitivity. The symmetry detection methods we propose do require sensors that are somewhat small, such that the field gradients over the sensor are not too large, but classical Hall effect sensors as used in smartphone compasses seem appropriate.

For above mentioned capacitive currents, however, relevant magnetic fields can be around single digit nT, which could require more sensitive sensors to detect. Additionally, with small signals like that it is not straightforward to distinguish them from background noise from the other cables, which are in close proximity. Particularly for such small signals, quantum sensors could offer benefits.

Hence, we briefly comment on the state-of-the-art of currently existing quantum magnetometers based on the expected magnetic field strengths. Established quantum magnetometry technologies are optically pumped magnetometers (OPMs), nitrogen-vacancy (NV) centres in diamond, and Superconducting quantum interference devices (SQUIDs). We do not consider SQUIDs, as they require cryogenics and are not very portable, which is a requirement for the cable selection use case.

- **Optically pumped magnetometers.** OPMs are a type of quantum magnetometer based on atomic vapour. These sensors can exhibit a very high sensitivity down to the femto Tesla (fT) [5]. OPMs are also relatively small (compared to other quantum magnetometers) and

their TRL (technology readiness level) is 9, so there are already commercial OPMs available for purchase, e.g. [6] and [7]. However, for common cable selection workflows, we expect the typical field range of OPMs to be too low. The highest dynamic range we are aware of is $\sim$150 µT, which could potentially be exceeded when close to the cable ($>$100 µT from the cable and an additional $\sim$50 µT from the earth magnetic field). Hence, OPMs are less likely to be applicable for common cable selection tasks. For capacitive current measurements, however, OPMs could certainly detect the required single digit nT signals, so they could be of interest for such a task.

- **Nitrogen-vacancy centres.** NV centres in diamond are sensitive to magnetic fields, operate at room temperature and can be read out optically, making them very versatile for various applications. The best portable setups can reach a sensitivity in the pico Tesla (pT) range, e.g. the set up by Bosch [8], which is more than enough for cable selection and should also suffice for capacitive current measurements. More importantly, NV centres can exhibit a higher dynamic range up to a few mT, see e.g. [9], which is sufficient for cable selection in a realistic setting.

3 Load Detection

3.1 Problem definition

The problem of load detection is the problem of detecting the load on a cable in a *non-invasive* manner, i.e., without digging up the cable. The application area is energy fraud, as load detection can be used for identifying unusually high currents running to a location.

The simplest setting of load detection is therefore a single underground cable running from a main line cable to a house. The question to be answered is: what is the load on that cable? To determine this, one only wants to measure above ground. The goal is therefore to detect the magnetic field induced by the 50-Hz currents that are running on the cable and from that deduce the current strength. A few variables make this challenging:

- The unknown depth of the cable, typically ranging between 40 cm to 1 m, which also influences the magnetic field strength. Hence, it can be hard to tell if a stronger magnetic field is due to a higher load on the cable or because the cable is located at a more shallow depth.
- The unknown balance between the three phases which can affect how the magnetic field propagates over distance.
- We assume only one cable running from the main line to a house but if other cables are present in the vicinity, their magnetic field might interfere with the cable that we are measuring.
- It might not be clear what phases are running on the cable and how well they are balanced. The cable could be a single phase cable or a 3-phase balanced cable, which in both cases would give a predictable magnetic field strength, albeit significantly weaker for the balanced cable. But one could also have multi phase cables that are out of balance in terms of their phase, or in terms of the current they are carrying. If this is unknown, it can be much more difficult to make sense of the magnetic field measured above ground.

3.2 Understanding magnetic fields away from the cable

The situation for load detection is as follows: We know the location of a buried low voltage cable and we want to measure the load on this cable from above the ground. The requirement is to resolve current differences of around 50 A and we can assume a depth between 50 - 100 cm, but it might not be clear how deep exactly the cable is buried. We assume little to no interaction of other cables as the cable in question is assumed to be somewhat isolated. For simplicity, we also assume no shielding of the magnetic field by the cable in this section. Shielding factors are different per cable type, and Alliander simply assumes a general shielding of 50%.

To estimate the fields we would need to be able to measure, we are using Ampère's law, given by

$$B(I, r) = \mu_0 \frac{I}{2\pi r}, \tag{3.1}$$

where I is the current in A and r the distance in m. This formulation is for a single wire carrying current. Note that in this formulation the current is constant and we need to handle the alternating current 'manually', so we adapt the current by multiplying with the phase $\cos\phi$. For a single wire cable, we can directly use this formula to obtain the expected magnetic field strength at a given sensor distance and current. For a three phase balanced cable, the setup looks as depicted in Figure 3.1. We typically use r to denote the distance from the sensor to the cable, where we mean the distance to the top wire, so $r_1 = r$. The other two distances are then given by

$$r_{2,3} = \sqrt{r^2 + d^2 - 2rd\cos(\frac{5}{6}\pi)} = \sqrt{r^2 + d^2 + \sqrt{3}rd}, \tag{3.2}$$

using the law of cosines. The resulting magnetic field strength at the sensor is given by

$$B(I, r) + B(I \cdot \cos(\frac{2}{3}\pi), r_2) + B(I \cdot \cos(\frac{4}{3}\pi), r_3), \tag{3.3}$$

so we offset the phases on each wire by $\frac{2}{3}\pi$. However, for the 3-wire situation, it might be too much of a simplification to leave out the vector component of the fields. So we also consider the vectorised version, where each of those scalars is multiplied with the unit vector pointing in the direction of the field. These vectors can be determined by simply finding an orthogonal vector to the vector between the cable and measurement location, and choosing the correct one based on the right hand rule. We denote those unit vectors by $\vec{b}_1, \vec{b}_2$, and $\vec{b}_3$, for the three wires respectively. Then the strength of the magnetic field is given by the norm of the sum of those vectors:

$$\left\| B(I, r) \cdot \vec{b}_1 + B(I \cdot \cos(\frac{2}{3}\pi), r_2) \cdot \vec{b}_2 + B(I \cdot \cos(\frac{4}{3}\pi), r_3) \cdot \vec{b}_3 \right\|, \tag{3.4}$$

All calculations can be found in the accompanying Jupyter notebook (Appendix A). As a sanity check, we compared the simplified scalar equation and the vector version in Figure 3.2 and as we can see, the vectorised version results in slightly stronger magnetic fields. This is to be expected, as the fields from the different wires point in different directions, which results in slightly worse cancellation of the fields. The differences become negligible with increasing stand-off distance. From now on, we only use the vectorised version when considering triple cables.

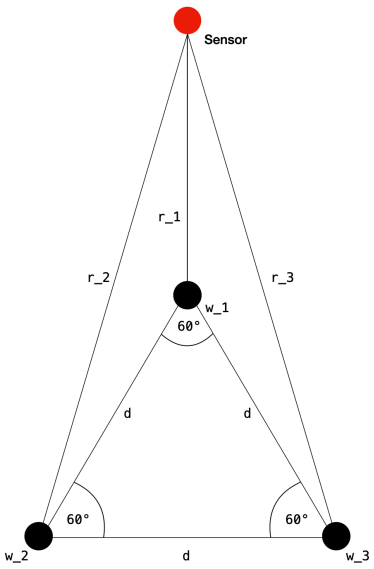

Figure 3.1: 3-Phase balanced cable set up. w_1, w_2 and w_3 are the three wires of the cable.

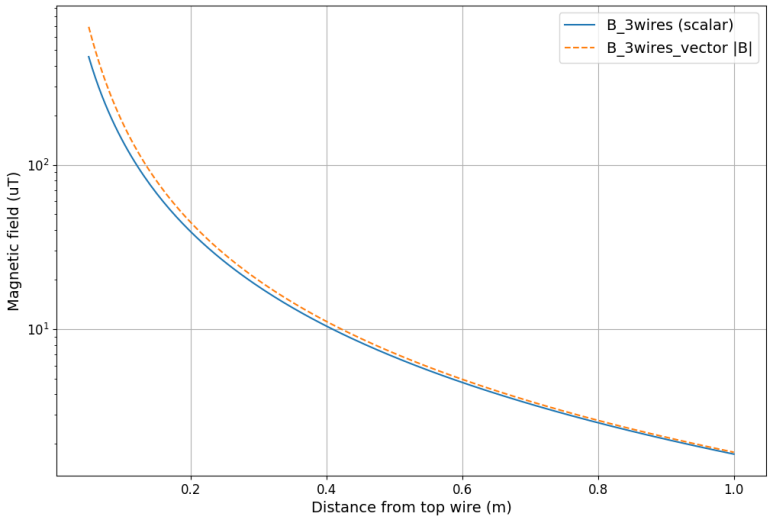

Figure 3.2: Magnetic field strength for three phase cables over distance, comparing the simplified scalar equation and the vectorised equation.

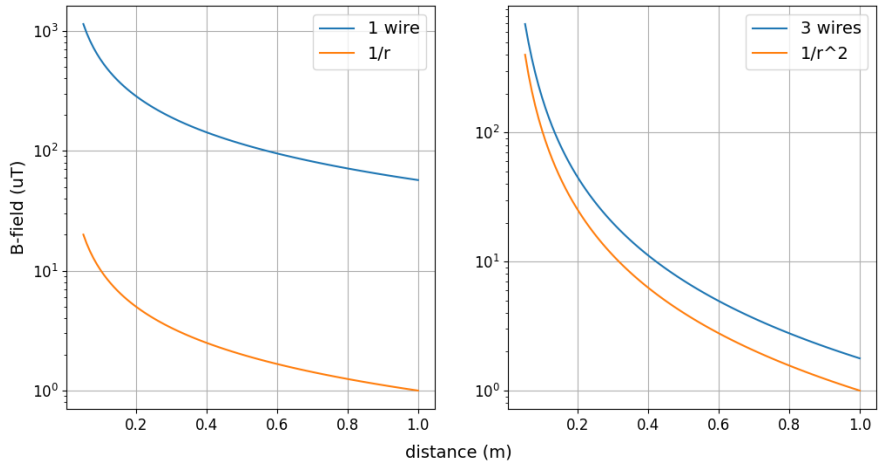

Figure 3.3: Magnetic field strength over distance for single (left) and three (right) phase cables, using a current of 285 A.

3.2.1 Magnetic field strengths

When computing the expected magnetic fields with Equation (3.1) and Equation (3.3), we see that the fields fall off over distance according to $\frac{1}{r}$ and $\frac{1}{r^2}$ respectively, see Figure 3.3. In Table 3.1 and Table 3.2 we collected the expected magnetic field strengths for different currents and distances, considering single and triple cables respectively.

3.3 Inferring currents and depths

In a real-world setting, we would like to be able to infer the current on the cable by measuring the magnetic field above ground. We assume that we can locate the position of the cable in the ground (by simply 'scanning' across the ground and finding the highest magnetic field value), so we can assume that the sensor can be placed vertically above the cable. However, we do not know how deep the cable is buried, so we are using two sensors to also obtain the gradient information of the field. The setup is then as described in Figure 3.4.

Current(A)	0.4 m	0.6 m	0.8 m	1.0 m	1.2 m	1.4 m
10	5.00	3.33	2.50	2.00	1.67	1.43
20	10.00	6.67	5.00	4.00	3.33	2.86
30	15.00	10.00	7.50	6.00	5.00	4.29
40	20.00	13.33	10.00	8.00	6.67	5.71
50	25.00	16.67	12.50	10.00	8.33	7.14
60	30.00	20.00	15.00	12.00	10.00	8.57
70	35.00	23.33	17.50	14.00	11.67	10.00
80	40.00	26.67	20.00	16.00	13.33	11.43
90	45.00	30.00	22.50	18.00	15.00	12.86
100	50.00	33.33	25.00	20.00	16.67	14.29
150	75.00	50.00	37.50	30.00	25.00	21.43
200	100.00	66.67	50.00	40.00	33.33	28.57
250	125.00	83.33	62.50	50.00	41.67	35.71

Table 3.1: Expected magnetic field strength in µT based on distance and current for a **single wire cable**.

Current(A)	0.4 m	0.6 m	0.8 m	1.0 m	1.2 m	1.4 m
10	0.390	0.173	0.097	0.062	0.043	0.032
20	0.780	0.347	0.195	0.125	0.087	0.064
30	1.171	0.520	0.292	0.187	0.130	0.095
40	1.561	0.693	0.390	0.249	0.173	0.127
50	1.951	0.867	0.487	0.312	0.217	0.159
60	2.341	1.040	0.585	0.374	0.260	0.191
70	2.732	1.213	0.682	0.437	0.303	0.223
80	3.122	1.386	0.780	0.499	0.346	0.255
90	3.512	1.560	0.877	0.561	0.390	0.286
100	3.902	1.733	0.975	0.624	0.433	0.318
150	5.853	2.600	1.462	0.936	0.650	0.477
200	7.804	3.466	1.949	1.247	0.866	0.636
250	9.756	4.333	2.437	1.559	1.083	0.795

Table 3.2: Expected magnetic field strength in µT based on distance and current for a **balanced triple wire cable**.

For the case of a single wire we get two equations based on the two measurements M_1 and M_2 at sensors S_1 and S_2, namely

$$M_1 = B(I, r) \tag{3.5}$$
$$M_2 = B(I, r + ds) \tag{3.6}$$

which we can solve for r and I, since ds is known. This yields

$$r = \frac{ds}{\frac{M_1}{M_2} - 1}, \tag{3.7}$$
$$I = M_1 \cdot r \cdot \frac{2\pi}{\mu_0}, \tag{3.8}$$

so it is straightforward to deduce the current and distance from the two measurements. For

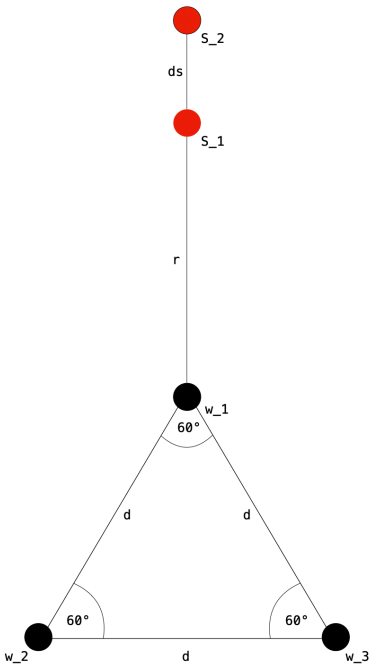

Figure 3.4: Sensor set up for a three phase cable. For a single phase cable we simply ignore w_2 and w_3.

the case of a triple cable we get the following two equations:

$$M_1 = B(I, r) + B(I \cdot \cos(\frac{2}{3}\pi), r_2) + B(I \cdot \cos(\frac{4}{3}\pi), r_3) \tag{3.9}$$

$$M_2 = B(I, r + ds) + B(I \cdot \cos(\frac{2}{3}\pi), \hat{r}_2) + +B(I \cdot \cos(\frac{4}{3}\pi), \hat{r}_3), \tag{3.10}$$

where r_2 and r_3 denote the distances from S_1 to w_2 and w_3, and $\hat{r}_2$ and $\hat{r}_3$ denote the distances from S_2 to w_2 and w_3, so $\hat{r}_{2,3} = \sqrt{(r + ds)^2 + d^2 + \sqrt{3}(r + ds)d}$. This system may be solvable analytically, but for simplicity we do it numerically.

In both cases, we are able to accurately return the load and distance with only having access to the measurement values, as can be verified in the accompanying Jupyter notebook (Appendix A).

3.4 Insights and recommendations

As we did before for cable selection, we will now discuss our findings. Again, these insights come from our technical point of view and might not always be fully applicable to the operational scenarios encountered at Alliander.

3.4.1 Technical feasibility

As we have seen in Table 3.1, the expected magnetic fields for single-wire cables are still in the µT range, even for low currents of 10 A and distances of up to 1.4 m. This is easily measurable with conventional magnetometers. For balanced three-phase cables the lowest expected values are ∼30 nT, which is still somewhat comfortably detectable by, e.g., the Maschek ESM-100 Fieldmeter [10] that Alliander has in possession. The device that is currently used by

Alliander technicians to detect cables underground is made by Vivax-Metrotech [11], which consists of 12 magnetometers, split up into sets of 6 which are at different distances from the cable. Hence, it acquires gradient information to estimate load and depth of the cable simultaneously. It can be tuned to specific AC frequencies which are put on the cable via a transmitter. Then the device is able to locate the cable and give estimates for depth and load. However, as we learnt from Alliander technicians, it can only give the load component for frequencies unequal to 50 Hz. It cannot display the load on a cable when searching for 50 Hz signals, so there must be an underlying issue preventing it to do so.

We expect this issue for in-field load detection to stem from a simplification that we have made, namely that there is no background noise. We assume that the Vivax-Metrotech device is able to confidently state the load for frequencies outside of 50 Hz, as it assumes there are no other sources with that exact frequency. For 50 Hz, however, it cannot generally make that assumption as the whole electricity network runs on 50 Hz. The difficulties stemming from this background noise were also apparent in the field measurements we have done at the test location of Alliander, which we discuss in Section 4.3.

Theoretically, one should still be able to resolve this issue by using the gradient information collected by multiple sensors with some distance between them. This, however, would require a certain knowledge about the situation. We can, e.g., envision algorithms (see, e.g., [12]) that could cancel out background noise based on the different drop-off rates of the fields of different sources, under the assumption that the cable that needs to be measured is the closest cable to the sensors (i.e., the source with the highest drop-off rate).

Another issue can occur in the case of three-phase cables. We assumed in the previous section that the loads are equally distributed and the phases are balanced. This gives us a clear formula to determine the expected magnetic field as well as the expected drop-off over distance. If, however, the phases are out of balance or the load is not equally distributed, this formula does not hold anymore. This issue becomes even worse when there is also current on the null phase.

If the magnetic shielding of the cable is unknown, the deduction of the load on the cable is complicated further; this makes it unclear if a weaker magnetic field is due to a lower load or due to a better shielding.

› Hence, we conclude that the difficulties associated with load detection stem primarily from a data analysis challenge, namely the reconstruction of the load given the measurements. New sensors could still help by providing more (detailed) data, which could aid in solving the data analysis challenge.

3.4.2 Applicability of quantum sensors

As discussed at the end of the previous section, both improved sensors and improved data analysis algorithms can play an important role in realising load detection.

A quantum magnetometer could improve sensitivity of the sensor. This is currently not the main limitation for load detection. If, however, also smaller currents need to be resolved, or the stand-off distance to the cable is larger, or the cable shields magnetic field better, then the expected magnetic fields could be a few nanotesla. This low field strength, in combination with a requirement for a wide dynamic range and the ability to resolve 50 Hz, could be challenging for classical magnetometers and therefore potentially applicable for NV-centre based magnetometers.

NV centre based magnetometers could also improve the accuracy of the vectorial information of the field, as the diamond-lattice gives inherent vector capabilities. We are, however, unsure how relevant such an improvement would be. It could potentially support in distinguishing signal from noise, or help in 'guiding' towards the cable, but we would assume that an arrangement of three or more conventional small scale sensors can also achieve sufficient vectorial accuracy.

Generally, for load detection, it will be important to gather a lot of data at different locations to faithfully reconstruct the load on a cable. Ideally, a sensor solution would therefore measure at different positions simultaneously. A quantum magnetometer could be relevant here, since the small size of the sensor head allows for the realisation of a distributed sensor system (with many sensors at different locations). This, as mentioned above, would then have to be combined with advanced data analysis in order to reconstruct the load.

4 Lab and Field Tests

In this chapter, we will discuss the measurements done using the quantum sensor developed at the TNO High Tech Industry Unit. The goal of these measurements was to verify the feasibility of measuring 50 Hz magnetic fields using a quantum sensor with the eventual goal of translating this to the current running through an underground cable. Here, we mainly tackle the first question.

4.1 Technology

The quantum sensor developed at TNO is based on nitrogen-vacancy (NV) centres in diamond. A detailed discussion of nitrogen-vacancy centres and their use as magnetometers can be found in literature [13, 14]. Here, we will discuss some basic principles, but this is not meant to be exhaustive.

The NV centre is a crystallographic defect in diamond, where two carbon atoms are replaced by a nitrogen atom and a vacancy. Manipulation of the nitrogen-vacancy centres using a green (515 nm) laser and microwaves ($\sim$ 2.8 GHz) allows their use as sensitive magnetic field sensors. There are four different NV families inside the diamond, belonging to four different orientations of the NV centres. Each NV centre is a spin-1 system, which implies there are two allowed ground-state transitions that can be excited using microwaves at $\sim$ 2.8 GHz. In Figure 4.1, we show the eight (4 families $\times$ 2 transitions per family) transitions, each at a different radio-frequency (RF) frequency. Upon a changing external magnetic field, these transitions move left / right. Measuring this change allows us to reconstruct the external magnetic field.

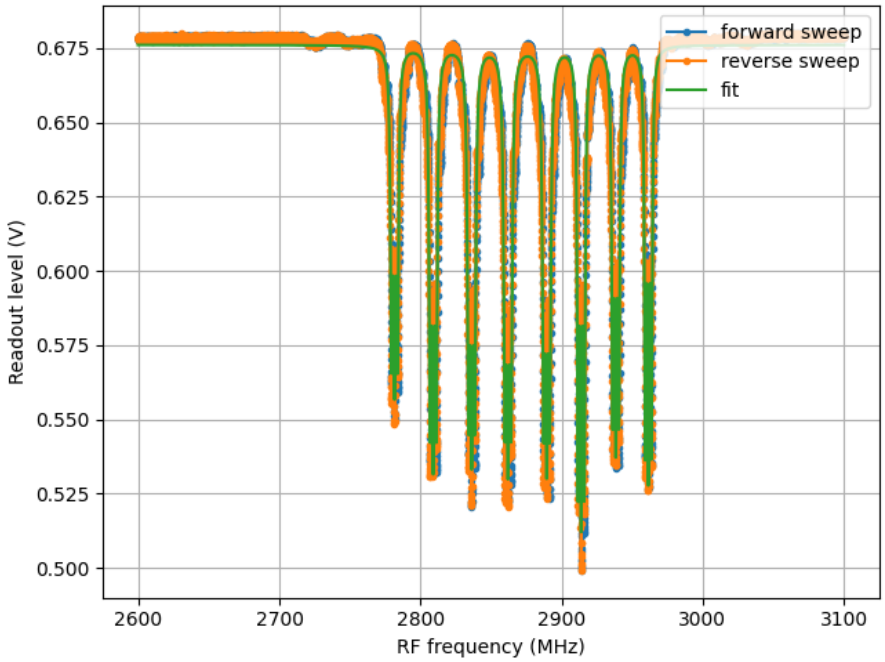

Figure 4.1: Pulsed optically-detected magnetic resonance (ODMR) measurement.

In order to measure 50 Hz oscillating magnetic fields using this sensor, we sequentially perform Ramsey measurements [13, 14] on each resonance. Information on the projection of the magnetic field on each of the four families allows us to reconstruct the full vector magnetic field, even when it is oscillating at 50 Hz.

4.2 Lab measurements

To demonstrate the ability to measure 50 Hz oscillating magnetic fields, we perform a number of lab experiments with the setup shown in Figure 4.2. We run a variable 50 Hz current through a two-wire cable with a phase difference between the two wires of 180 degrees. First, we run the cable parallel to the optical axis of the nitrogen-vacancy setup (Figure 4.3). When varying the current in the cable, we observe a linear output of the total magnetic field, as expected. In Figure 4.4, the cable runs perpendicular to the optical axis of the nitrogen-vacancy setup. Here, we also observe a linear dependence, as expected. Note that the absolute total magnetic field numbers are different between Figure 4.3 and Figure 4.4, since the stand-off distance between the diamond and cable is different.

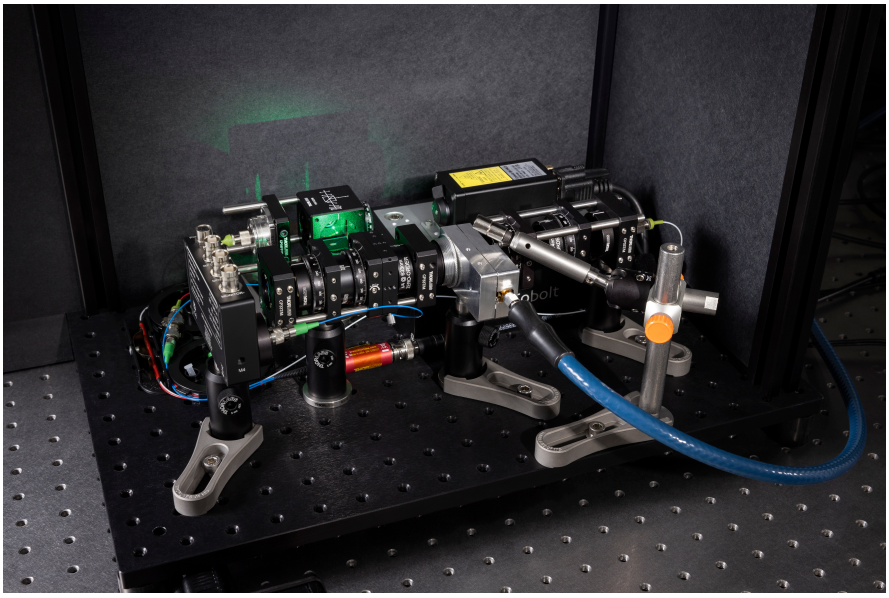

Figure 4.2: Picture of the nitrogen-vacancy quantum sensor. For the lab measurements, we positioned a cable over this setup.

In the lab we also performed similar measurements using a cable from Alliander. For these experiments, we used a single-phase cable and changed the 50 Hz current running through the cable. In Table 4.1 and Table 4.2 the results for two different orientations of the cable with respect to the quantum sensor are shown. We find that doubling the current approximately doubles the magnetic field components, which is what one would expect. Furthermore, the magnetic field components are as expected given the orientation of the cables with respect to the quantum sensor. This suggests that these magnetic field vector measurements can be used to locate the cable.

Finally, we have performed measurements using a varying frequency on a cable. These measurements (not shown) showed that we can distinguish small frequency variations, i.e. the difference between 50.0 Hz and 50.1 Hz can be measured with a 10 s integration time. The frequency variation one is able to distinguish, will generally be limited by the integration time (1/10 s = 0.1 Hz). Importantly, it is not limited by the noise or drift of the quantum sensor.

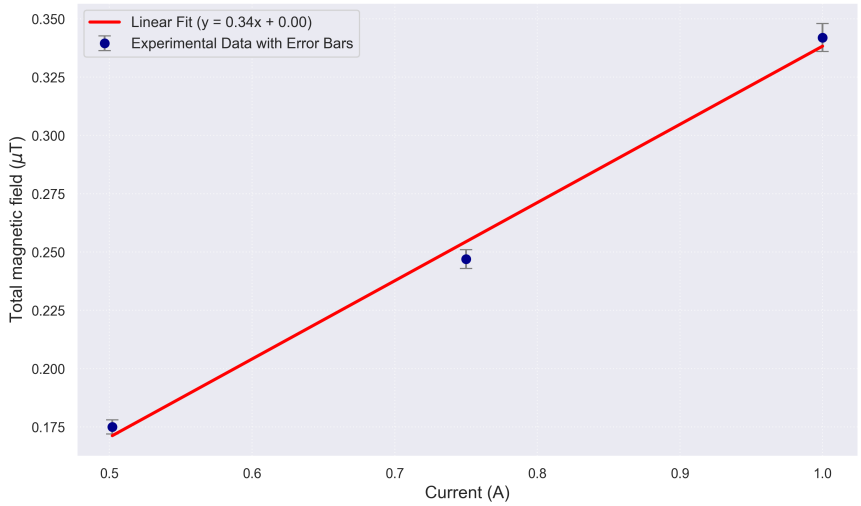

Figure 4.3: Measured total 50 Hz magnetic field magnitude versus the applied current when the cable is parallel to the optical axis.

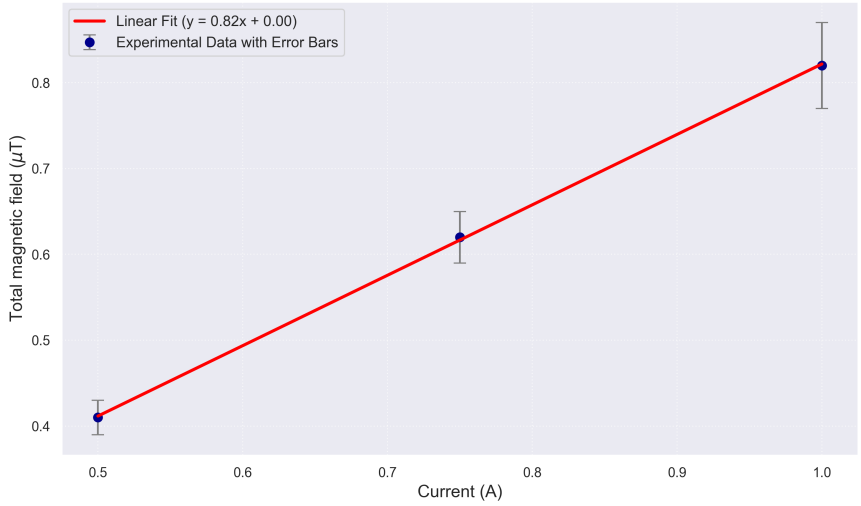

Figure 4.4: Measured total 50 Hz magnetic field magnitude versus the applied current when the cable is perpendicular to the optical axis.

4.3 In-field measurements

For the final phase of the project, we performed measurements in the field at a location of Alliander. In Figure 4.5, we schematically show the local situation. A container, containing a total of 19 lamps, draws currents of up to 75 A (balanced over three phases with up to 25 A loads per phase) through a low-voltage cable (LV) that is connected to the main net, which runs along the road. The cable is approximately 60 cm deep. The current running through the low-voltage cable can be varied by turning on/off lamps in the container.

We performed magnetic field measurements at the positions (“sensor position 1” and “sensor position 2”). The first sensor position was chosen as the location of the cable was very well known at this spot. The second location was determined by trying to follow the magnetic field of the cable using the Maschek Fieldmeter from Alliander. At the first sensor position, we

	100.2 mA	201.2 mA
B_x	17(4)	41(10)
B_y	44(4)	98(9)
B_z	260(4)	516(10)
B_{total}	264(4)	527(10)

Table 4.1: Magnetic field measurements (columns) for the magnetic field vector components in nT when the Alliander cable is perpendicular to the optical beam path for varying currents. The number in brackets denotes the error bar on the last digit.

	100.0 mA	200.9 mA
B_x	198(3)	369(7)
B_y	108(3)	220(8)
B_z	12(3)	61(8)
B_{total}	225(3)	434(7)

Table 4.2: Magnetic field measurements (columns) for the magnetic field vector components in nT when the Alliander cable is parallel to the optical beam path for varying currents. The number in brackets denotes the error bar on the last digit.

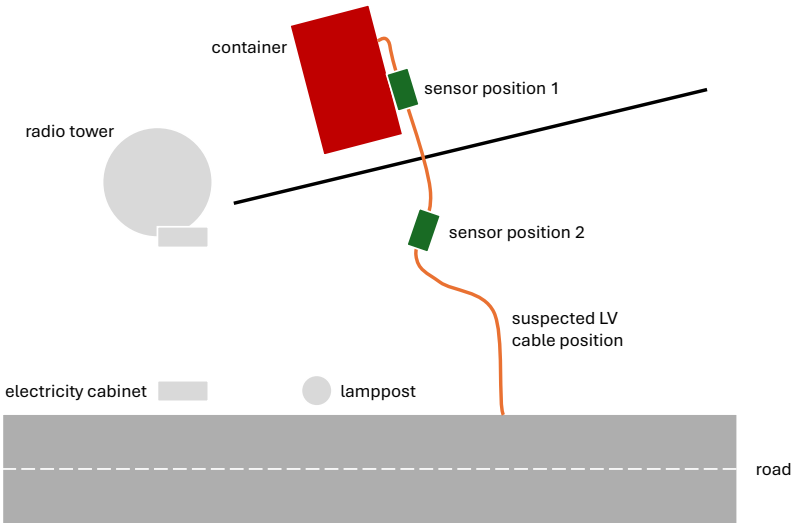

Figure 4.5: Sketch of the situation at Alliander's site. The suspected position of the low-voltage (LV) cable was determined through a combination of drawings, the engineers' knowledge of the cable position and our own determination using the Maschek Fieldmeter. Magnetic fields close to and under the radio tower were measured to be negligible ($< 500nT$) compared to the fields measured at the sensor positions.

measured significant magnetic fields ($\sim$ µT). These measurements were in agreement with the Maschek Fieldmeter. After further investigation, the magnetic field turned out to mainly originate from the wall of the container rather than from the low-voltage cable. Magnetic fields of tens of µT were measured at a height of $\sim$ 50 cm on the outside wall of the container, likely originating from electronics associated with a set of three lamps. This complicates the interpretation of the measurements measured at this location, so in the following we will focus on sensor position 2.

At sensor position 2, we performed magnetic field measurements while varying three param-

eters: the height of the setup from the ground, the rotation of the setup with respect to the cable and the current that the container draws. We will now discuss these in order.

4.3.1 Height

In Figure 4.6, we show the measured total magnetic field as a function of the height of the setup from the ground. At each height, we measure three times, hence there are three data points per sensor height. In Figure 4.6, we see that the magnetic field goes down as we move the setup up, which is as expected. However, we would expect the behaviour to follow a $1/r$ (single-phase current) or $1/r^2$ (three-phase current) curve, which it does not (Figure 4.6). This could be because it is practically hard to move the setup just vertically. Any accidental lateral movement and/or rotation may explain the observed deviation. Another complicating factor is the fact that the three phases of the cable are not perfectly balanced (22.2 A, 25.4 A, 23.0 A over the three phases).

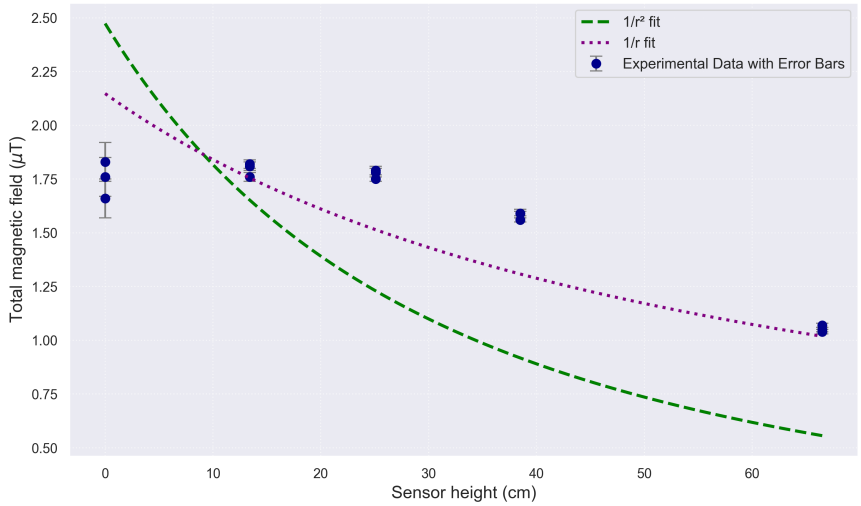

Figure 4.6: **Total magnetic field as a function of sensor height.** The current decreases as we increase the height of the setup, which is expected. However, one would expect the behaviour to follow a $1/r$ (single-phase current) or $1/r^2$ (three-phase current) curve, which it does not. To demonstrate this, we fit the data to $a/(r+60)$ (green, $a \approx 129$) and $b/(r+60)^2$ (purple, $b =\approx 8905$).

4.3.2 Rotation

Next, we rotated the setup by 90 degrees either way to observe the effect on measured magnetic field vector components. In Table 4.3, 4.4, and 4.5, we show the results for a setup rotation of 0, -90, +90 degrees respectively. For each configuration, we perform three measurements. In this case, all lamps in the container were on and it was drawing 22.2 A, 25.4 A, 23.0 A over the three phases.

First, we find that the three repetitions of the measurements are in agreement with each other. In Table 4.3, we find a small upwards trend and in Table 4.5 the final measurement is an outlier. For these cases, the current that the container was drawing did not change, but other environmental factors may have contributed to these changes.

Second, we find that the results in Table 4.4 (-90) and Table 4.5 (+90) are qualitatively similar. The exact numbers differ, since we do not achieve a perfect 180 degree rotation and we may have introduced unwanted lateral movement. Broadly speaking though, the B_x, B_y and B_z components are the same between -90 degrees and +90 degrees, which is expected.

	Measurement 1	Measurement 2	Measurement 3
B_x	1.4(1)	1.47(9)	1.5(1)
B_y	0.65(5)	0.69(6)	0.71(6)
B_z	0.65(7)	0.68(6)	0.71(7)
B_{total}	1.66(9)	1.76(8)	1.83(9)

Table 4.3: Three magnetic field measurements (columns) for the magnetic field vector components in μT when the setup is at 0 degrees with respect to the suspected low-voltage cable. The number in brackets denotes the error bar on the last digit.

	Measurement 1	Measurement 2	Measurement 3
B_x	1.24(3)	1.24(3)	1.23(3)
B_y	0.82(2)	0.81(2)	0.79(2)
B_z	1.77(3)	1.75(3)	1.72(3)
B_{total}	2.31(3)	2.29(3)	2.26(3)

Table 4.4: Three magnetic field measurements (columns) for the magnetic field vector components in μT when the setup is at -90 degrees with respect to the suspected low-voltage cable. The number in brackets denotes the error bar on the last digit.

	Measurement 1	Measurement 2	Measurement 3
B_x	1.46(6)	1.44(6)	1.25(6)
B_y	0.80(4)	0.78(4)	0.67(3)
B_z	1.77(5)	1.73(5)	1.50(4)
B_{total}	2.43(5)	2.38(5)	2.07(5)

Table 4.5: magnetic field measurements (columns) for the magnetic field vector components in μT when the setup is at +90 degrees with respect to the suspected low-voltage cable. The number in brackets denotes the error bar on the last digit.

Third, between the result for 0 degrees (Table 4.3) and either of the results for $\pm$ 90 degrees (Table 4.4 and 4.5), we would expect the x and z components to interchange. We observe that in Table 4.4 and 4.5 the z component is largest and in Table 4.3 the x component is largest. However, it is hard to draw more than qualitative conclusions due to the significant difference in magnitude of the components, which we contribute to unwanted lateral movement / rotation of the setup.

In conclusion, these results show that the measured magnetic field vector is in agreement with our expectations based on the rotation of the quantum sensor. This in principle allows us to infer the cable direction.

4.3.3 Current

The final parameter we varied, was the current the container is drawing. In Figure 4.7, we plot the measured magnetic field as a function of the total current, summed over three phases. For the rightmost points, the currents over the phases were: 22.2 A, 25.4 A, 23.0 A. For the middle points: 11.7 A, 12.0 A, 10.8 A. For the leftmost points: 0.3 A, 0.0 A, 1.9 A. The leftover current for the leftmost points is mostly coming from the current the nitrogen-vacancy quantum sensor equipment draws, since it is connected to power in the container.

First, we discuss the total magnetic field, which measures around 2 μT. In simulation, we find that 25 A on each phase would result in a magnetic field of $\sim$0.4 - 0.5 μT, assuming perfect balancing and no magnetic field shielding due to the cable exterior. For a current of 3 A on a single phase, we would expect a magnetic field of $\sim$1 μT, again assuming no magnetic

field shielding due to the cable exterior. This suggests that the measured magnetic field is mostly coming from the unbalanced currents over the cable. A more comprehensive analysis should include the current in the null cable and calculate the expected magnetic field for an unbalanced three-phase cable.

Second, we discuss the trend in Figure 4.7. We observe that the measured total magnetic field does not change when the current drawn by the container is changed. One would have expected the total magnetic field to reduce when the current goes down. We now discuss some possible reasons for this discrepancy:

- *The quantum sensor does not measure the magnetic field accurately.* This is unlikely, since we regularly cross-checked the quantum sensor measurements with the Maschek Fieldmeter measurements, and always found good agreement.
- *We are not measuring the magnetic field from a cable.* This is unlikely, since moving the Maschek Fieldmeter laterally or vertically away from the "cable" along the length of the cable shows reduced fields. This strongly suggests that there is a cable with current running underground along that line. However, following the "cable" with the Maschek Fieldmeter showed quite some variation in magnetic field strength, from ∼1 µT to 5 µT, which indicates potential other sources of magnetic field.
- *The container is always drawing max. current.* This may be possible, but it is unclear how. Namely, the current over the three phases is measured independently in the container.
- *A large rest current is running over the cable.* This is possible. However, to generate a magnetic field of 2 µT at a distance of 60 cm, one would need a current of 6 A over a single phase. This seems unlikely.
- *The observed total magnetic field is mostly coming from the unbalanced currents on the phases and null cable.* This is possible, since the phases are unbalanced by a few Ampère. However, the absence of any clear changes in the data is still surprising, given that a change in current would lead to a change in balancing of the phases and consequently a change in the measured total magnetic field.

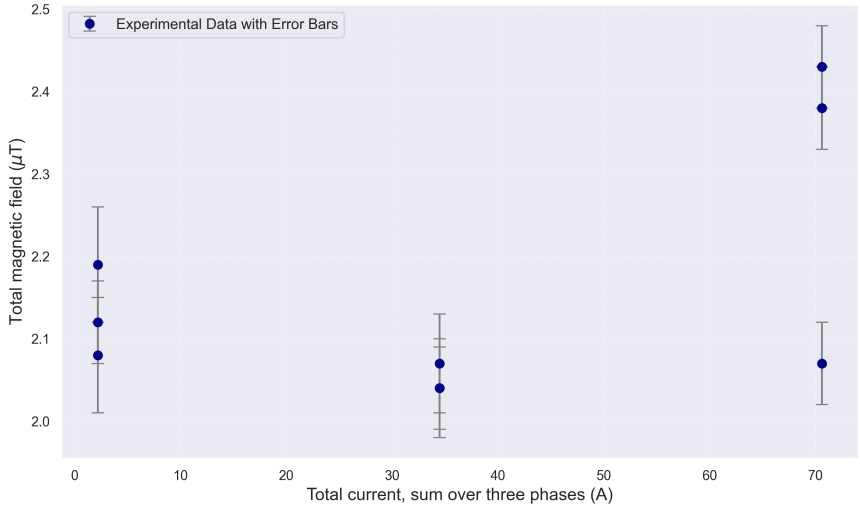

Figure 4.7: Total magnetic field as a function of the total current running through the low-voltage cable. For the rightmost points, the currents over the phases were: 22.2 A, 25.4 A, 23.0 A. For the middle points: 11.7 A, 12.0 A, 10.8 A. For the leftmost points: 0.3 A, 0.0 A, 1.9 A. For each current, we perform three measurements.

4.3.4 Pictures from field measurements

In this section, we collect some photos from the field measurements for reference.

(a) (b)

Figure 4.8: (a) The situation in the field. The container draws up to ∼75 A. The two boxes in the front host the quantum sensor and the equipment to operate the quantum sensor. (b) Running a measurement with the quantum sensor using the laptop as an interface. The sensor is located at sensor position 1 in this picture.

Figure 4.9: Running a measurement at sensor position 1.

Figure 4.10: Running a measurement with the quantum sensor using the laptop as an interface. The sensor is located at sensor position 2 in this picture.

Figure 4.11: The inside of the container.

5 Discussion

This project explored the potential of quantum sensing for cable selection and load detection in power distribution networks, focusing on both theoretical modelling and practical measurements.

For cable selection, the results indicate that the magnetic fields close to the cable are typically strong enough (∼100 µT) to be measured by conventional sensors. The difficulties arising in selection tasks seem to stem more from procedural and operational difficulties than from technical limitations of classical sensor technology. The symmetry-based identification methods that we proposed could most likely be implemented with classical sensors, provided they are sufficiently small. However, quantum magnetometers, particularly those based on NV centres or OPMs, could offer advantages in miniaturisation of magnetic-field sensors and in scenarios where signals are weak, such as detecting capacitive currents in turned-off, but still connected, cables, which we expect to produce magnetic fields potentially as low as a few hundred pT. However, these capacitive current measurements are not currently done at Alliander, so we cannot comment how well they would fit in Alliander's operations and processes.

Therefore, for cable selection, we conclude the importance of:

- A **clear readout device** for current selection processes, by, e.g., switching to a digital readout.
- Further investigating the applicability and feasibility of the **symmetry metric** and the **capacitive current measurements** in real-world cable selection tasks.
- Defining **processes for using smart secondary substations**, when they are available, to improve cable selection.

For load detection, we modelled the magnetic fields generated by underground cables using Ampère's law and were able to theoretically infer both current and cable depth from above-ground measurements. These methods assumed some simplifications about the vertical positioning of the sensor above the cable, and the absence of background noise. Luckily, as we mention above, these issues should be feasible to solve by using more sensors (gradient information) and more sophisticated data analysis. Other simplifications, however, namely the unknown shielding of the cable and, in the case of multi-phase cables, the unknown balance of the phases, pose challenges that might be harder to solve.

We also conducted experiments with our NV centre magnetometer. In the lab, we measured oscillating magnetic fields at 50 Hz coming from a simple cable, as well as from an original XLPE cable, to prepare for the field test at an Alliander test facility. Here, we were able to show that our quantum sensor is able to measure the relevant magnetic fields at 50 Hz under real-world conditions. We also encountered the difficulties of real-world load detection. While the measurements of the quantum sensor aligned well with those of the Maschek fieldmeter, the measured magnetic field values were not in line with our expectations.

Therefore, for load detection, we conclude the importance of:

- **Multiple sensors with sophisticated data analysis** to be able to cancel out background noise and to identify the various sources of magnetic field.
- A **clear user interface** that enables the technician to make sense of the measurements while in the field.

Hence, we believe that future work should focus on these points. Quantum sensors can come in for potential scenarios where high sensitivities and a small form factor are required, either for symmetry measures, capacitive current detection, or as a grid of sensors for load detection to enable advanced data analysis.

References

[1] *Cable tutorial series - COMSOL*. COMSOL.

[2] Phase to Phase. *Netten voor distributie van elektriciteit*. Phase to Phase, 2011. ISBN: 978-90-817983-1-0. URL: https://www.phasetophase.nl/boek/index.html.

[3] *Produktinformation – Bayka*. Accessed: 2025-05-06. Bayka AG. 2025. URL: https://www.bayka.de/productDocs/Produktinformation_EN.132927085.pdf.

[4] *Technical Data for Medium Voltage XLPE insulated cables*. EUPEN. URL: https://www.eupen.com/cable/wp-content/uploads/sites/2/EUPEN_Technical_Data_for_Medium_Voltage_XLPE_insulated_cables.pdf.

[5] William Fourcault et al. "Helium-4 magnetometers for room-temperature biomedical imaging: toward collective operation and photon-noise limited sensitivity". In: *Opt. Express* 29.10 (May 2021), pp. 14467–14475. DOI: 10.1364/OE.420031.

[6] *PPM Pulsed Pump Magnetometer*. Twinleaf. URL: https://twinleaf.com/magnetometers/PPM/.

[7] *QTFM Gen-2*. QuSpin. URL: https://quspin.com/qtfm-gen-2/.

[8] *Technology*. Bosch Quantum Sensing. URL: https://www.bosch-quantumsensing.com/technology/.

[9] Tianning Wang et al. "High-Dynamic-Range Integrated NV Magnetometers". In: *Micromachines (Basel)* (2024). DOI: 10.3390/mi15050662.

[10] *ESM-100 H/E Fieldmeter*. maschek. URL: https://www.maschek.de/en/products/esm-100-h-e-fieldmeter.

[11] *vLoc3-Pro Receiver*. Vivax-Metrotech. URL: https://vivax-metrotech.com/vivax-product/vloc3-pro/.

[12] Jia-yu Xu et al. "Virtual Gradiometer-Based Noise Reduction Method for Wearable Magnetoencephalography". In: *2nd International Conference on Computer Science, Electronic Information Engineering and Intelligent Control Technology (CEI)*. 2022, pp. 24–29. DOI: 10.1109/CEI57409.2022.9950167.

[13] John F. Barry et al. "Sensitivity optimization for NV-diamond magnetometry". In: *Rev. Mod. Phys.* 92 (1 Mar. 2020), p. 015004. DOI: 10.1103/RevModPhys.92.015004.

[14] John F. Barry et al. "Sensitive ac and dc magnetometry with nitrogen-vacancy-center ensembles in diamond". In: *Phys. Rev. Appl.* 22 (4 Oct. 2024), p. 044069. DOI: 10.1103/PhysRevApplied.22.044069.

Appendix A

Jupyter Notebook

The Jupyter notebook is uploaded on Zenodo and can be accessed via https://doi.org/10.5281/zenodo.18389351.

ICT, Strategy and Policy

Anna van Buerenplein 1
2595 DA Den Haag
www.tno.nl

TNO innovation for life